water

MDPI

Article

A Combined Landslide Displacement Prediction Model Based on Variational Mode Decomposition and Deep Learning Algorithms

Mengcheng Sun [1], Yuxue Guo [2,*], Ke Huang [1] and Long Yan [3]

[1] Powerchina Huadong Engineering Corporation Limited, Hangzhou 311122, China; sun_mc@hdec.com (M.S.); huang_k@hdec.com (K.H.)
[2] Institute of Water Science and Engineering, College of Civil Engineering and Architecture, Zhejiang University, Hangzhou 310058, China
[3] Research Institute of Geotechnical Engineering, Hohai University, Nanjing 210098, China; yanlong@hhu.edu.cn
* Correspondence: yuxueguo@zju.edu.cn

Abstract: Accurate landslide displacement prediction is an essential prerequisite for early warning systems aimed at mitigating geological hazards. However, the inherent nonlinearity and dynamic complexity of landslide evolution often hinder forecasting performance. Previous studies have frequently combined signal decomposition techniques with individual machine learning methods to enhance prediction reliability. To address the limitations and uncertainties associated with individual models, this study presents a hybrid framework for displacement forecasting that combines variational mode decomposition (VMD) with multiple deep learning (DL) methods, including long short-term memory neural network (LSTM), gated recurrent unit neural network (GRU), and convolutional neural network (CNN), using a cloud model-based weighted strategy. Specifically, VMD decomposes cumulative displacement data into trend, periodic, and random components, thereby reducing the non-stationarity of raw data. Separate DL networks are trained to predict each component, and the forecasts are subsequently integrated through the cloud model-based combination strategy with optimally assigned weights. The proposed approach underwent thorough validation utilizing field monitoring data from the Baishuihe landslide in the Three Gorges Reservoir (TGR) region of China. Experimental results demonstrate the framework's capacity to effectively leverage the strengths of individual forecasting methods, achieving RMSE, MAPE, and R values of 12.63 mm, 0.46%, and 0.987 at site ZG118, and 20.50 mm, 0.52%, and 0.990 at site XD01, respectively. This combined approach substantially enhances prediction accuracy for landslides exhibiting step-like behavior.

Keywords: Baishuihe landslide; displacement prediction; deep learning algorithm; weighted combination strategy

check for updates

Citation: Sun, M.; Guo, Y.; Huang, K.; Yan, L. A Combined Landslide Displacement Prediction Model Based on Variational Mode Decomposition and Deep Learning Algorithms. *Water* **2024**, *16*, 3503. https://doi.org/10.3390/w16233503

Academic Editor: Salvatore Ivo Giano

Received: 17 October 2024
Revised: 24 November 2024
Accepted: 3 December 2024
Published: 5 December 2024

Copyright: © 2024 by the authors. Licensee MDPI, Basel, Switzerland. This article is an open access article distributed under the terms and conditions of the Creative Commons Attribution (CC BY) license (https://creativecommons.org/licenses/by/4.0/).

1. Introduction

Landslides are a prevalent geological hazard that result in extensive damage and considerable loss of life annually, particularly in mountainous regions around the world [1,2]. Since the initial operation of the Three Gorges Reservoir (TGR), numerous landslides have been triggered or reactivated, mainly due to the interaction of complex geological conditions and external hydraulic forces, which pose substantial risks to local residents. Given that surface displacement is an intuitive indicator of landslide stability, accurately predicting displacement is critical for early warnings and risk assessments, and it serves as a key function in preventing and mitigating landslide disasters [3–5].

In recent years, significant advancements in landslide displacement prediction methods have been achieved, and these methods are primarily classified into physics-based models and data-driven approaches [6]. Grounded in physical mechanisms, physics-based models aim to capture the relationships between landslide geometry, triggering factors,

and deformation. However, landslide displacement evolution exhibits strong nonlinearity, driven by geological conditions, morphological features, and anthropogenic actions [7]. Consequently, the accuracy of physics-based models is often constrained by complex boundary conditions, variable physical parameters, and stringent application constraints. In contrast, data-driven models bypass theoretical derivation by directly mapping nonlinear deformation characteristics from on-site monitoring data using advanced statistical methods [8–10]. Advances in artificial intelligence (AI) have significantly boosted the efficiency of data-driven approaches. Algorithms, including artificial neural networks (ANNs), support vector regression (SVR), and extreme learning machines (ELMs), are extensively utilized in landslide displacement forecasting, consistently demonstrating superior performance [11–15]. Reservoir-induced landslides are dynamic systems that are continuously influenced by deformation states and time-varying factors. Consequently, it is crucial to update predictive models by incorporating recent data while eliminating outdated information [16]. Deep learning (DL) algorithms, which are adept at extracting temporal dependencies and retaining historical information, are particularly well suited for modeling nonlinear dynamic processes [17]. As a result, numerous newly developed dynamic forecasting models utilizing multiple DL networks have been successfully applied not only in landslide prediction but also in related fields, such as energy consumption and streamflow forecasting [18–21].

In addition to selecting appropriate forecasting models, predictive accuracy is heavily reliant on effectively addressing the non-stationary nature of displacement and impact factor sequences [22]. Previous studies have used various signal decomposition techniques, including discrete wavelet transform (DWT), ensemble empirical mode decomposition (EEMD), and singular spectrum analysis (SSA) methods, with advanced machine learning (ML)-based forecasting models [23–25]. Cumulative displacement data are decomposed into multiple components with distinct characteristics and then predicted individually. However, the unpredictable number of decomposed modes and the ambiguous physical meaning of each component often impede the effective mapping of these components to specific triggering factors [26]. Furthermore, the factors with significant seasonal variation are frequently overlooked. To address the challenges of processing complex and nonlinear signals, this study employs the variational mode decomposition (VMD) method due to its excellent ability to suppress mode mixing, handle noise effectively, and maintain computational efficiency. By adapting to data scales, VMD reduces raw displacement sequence non-stationarity and isolates both high- and low-frequency components linked to causal factors [11].

Recently, various predictive models have integrated single advanced ML algorithms with signal decomposition techniques [27,28]. Frequently utilized ML algorithms, including SVM, ELM, RNN, and LSTM, are often combined with decomposition methods such as EMD, CEEMD, and VMD to construct hybrid models. These models have shown significant effectiveness in predicting landslide displacement [13,29,30]. Given the diversity of algorithmic structures, individual prediction models have their own strengths and limitations [27]. In scenarios where multiple forecasting models are available, the adoption of a combined model is considered a robust approach to leverage the advantages of individual predictors [31]. For linear combination methods, optimal weighting coefficients are determined to minimize forecast errors. Numerous statistical approaches, swarm intelligence algorithms, copula methods, and entropy-weighted techniques have been rapidly developed for this purpose [32]. However, as forecast error properties may vary over time, the effectiveness of combined models with fixed weights is limited. Few studies have explored the dynamic adjustment of combination weights based on the distribution characteristics of the original forecasts [33,34].

This research presents a hybrid framework for landslide displacement forecasting that integrates VMD with multiple DL algorithms (LSTM, GRU, and CNN). The Baishuihe landslide, which exhibits typical reservoir-induced step-like deformation, was selected as the case study. The key external causal factors were identified, and the monitored

displacement data were decomposed into trend, periodic, and random components, while the triggering factor sequences were segmented into high- and low-frequency components via VMD. LSTM, GRU, and CNN models were then utilized to predict each displacement component separately, and the total displacement was reconstructed by aggregating each predicted component. Finally, the cloud model-based combination method was utilized to ascertain optimal weights and integrate individual model predictions, yielding the final cumulative displacement forecast.

This paper is arranged as follows: Section 2 outlines the methodology. Section 3 provides a case study. Experimental results and performance analysis are presented in Section 4. Section 5 discusses the implications of our findings, limitations, and delineates future directions. Finally, Section 6 concludes with a summary of key contributions.

2. Methodology

The methods employed in this research include VMD, three DL methods, and a cloud model-based weighted strategy. A detailed description of these methods is presented below.

2.1. Variational Mode Decomposition (VMD)

VMD is an adaptive decomposition algorithm, which can separate an input sequence $x(t)$ into multiple intrinsic modes $u_k(t)$, each characterized by a specific bandwidth [35]. The implementation process is as follows:

(1) The Hilbert transform is employed on each $u_k(t)$ to determine its unilateral frequency spectrum. (2) The frequency spectrum is translated to the baseband by modulating it with an exponential function aligned with the estimated center frequency. (3) The bandwidth is estimated by minimizing the $L2$ norm of the demodulated signal's gradient. Subsequently, the decomposition process is transformed into a constrained variational problem, described as follows:

$$\begin{cases} \min\limits_{\{u_k\},\{w_k\}} \left\{ \sum\limits_{k=1}^{K} \left\| \partial_t \left[\left(\delta(t) + \dfrac{j}{\pi t} \right) * u_k(t) \right] e^{-jw_k t} \right\|_2^2 \right\} \\ \text{s.t.} \sum_{k=1}^{K} u_k = x(t) \end{cases} \tag{1}$$

where $x(t)$ represents the input time series, u_k and w_k are the intrinsic modes and center frequencies. K refers to the modes' number.

The quadratic penalty term α and Lagrangian multiplier λ are incorporated in Equation (1). This optimization is performed according to Equation (2):

$$\begin{cases} \hat{u}_k^{n+1}(w) = \dfrac{\hat{x}(w) - \sum\limits_{i \neq k} \hat{u}_i(w) + \hat{\lambda}(w)/2}{1 + 2\alpha(w - w_k)^2} \\ \hat{w}_k^{n+1} = \dfrac{\int_0^\infty w \left| \hat{u}_k^{n+1}(w) \right|^2 dw}{\int_0^\infty \left| \hat{u}_k^{n+1}(w) \right|^2 dw} \\ \hat{\lambda}^{n+1}(w) = \hat{\lambda}^n(w) + \tau \left[\hat{x}(w) - \sum\limits_k \hat{u}_k^{n+1}(w) \right] \end{cases} \tag{2}$$

where n denotes the iteration number, τ is noise tolerance. $\hat{x}(w)$, $\hat{u}_k^{n+1}(w)$ and $\hat{\lambda}(w)$ represent the Fourier transforms of $x(t)$, $u_k(t)$ and $\lambda(t)$. The termination condition for optimization is specified in Equation (3).

$$\sum_k \frac{\left\| \hat{u}_k^{n+1} - \hat{u}_k^n \right\|_2^2}{\left\| \hat{u}_k^n \right\|_2^2} < \varepsilon \tag{3}$$

where ε is the convergence tolerance.

2.2. Deep Learning Algorithms

2.2.1. Long Short-Term Memory Neural Network (LSTM)

LSTM introduces internal memory cells within its hidden layers, effectively facilitating the modeling of long-term dependencies in sequential signals [36]. These memory cells regulate the information flow using three fundamental gate elements. Specifically, the forget-update mechanism is mathematically described as follows:

$$\begin{cases} i_t = \sigma(W_{ix}x_t + W_{im}m_{t-1} + b_i) \\ f_t = \sigma\left(W_{fx}x_t + W_{fm}m_{t-1} + b_f\right) \\ o_t = \sigma(W_{ox}x_t + W_{om}m_{t-1} + b_o) \\ c_t = f_t \cdot c_{t-1} + i_t \cdot tanh(W_{cx}x_t + W_{cm}m_{t-1} + b_c) \\ m_t = o_t \cdot tanh(c_t) \\ \hat{y}_t = f\left(W_{ym}m_t + b_y\right) \end{cases} \tag{4}$$

where x_t and $\hat{y}_t$ represent the input and output vectors, respectively. W stands for the weight matrix, and b refers to the bias vector. c_t and m_t represent the cell state and hidden layer state, respectively. $\sigma(\cdot)$ and $tanh(\cdot)$ correspond to the sigmoid activation and hyperbolic tangent functions.

2.2.2. Gated Recurrent Unit Neural Network (GRU)

GRU is a simplified and computationally efficient variant of LSTM [37]. To streamline the LSTM cell structure and improve training efficiency, GRU utilizes update gates (z_t) in place of the i_t and f_t, while the reset gate (r_t) governs the information flow within the network. The operational principles are formulated as follows:

$$\begin{cases} z_t = \sigma(W_{zx}x_t + W_{zm}m_{t-1} + b_z) \\ r_t = \sigma(W_{rx}x_t + W_{rm}m_{t-1} + b_r) \\ \widetilde{m}_t = tanh[W_{mx}x_t + W_{mm}(r_t \cdot m_{t-1})] \\ m_t = (1 - z_t) \cdot m_{t-1} + z_t \cdot \widetilde{m}_t \end{cases} \tag{5}$$

where x_t is the input vector. W stands for the weight matrix between each node. b represents the bias vectors. $\widetilde{m}_t$ and m_t denote the memory cell vector and hidden layer vector, respectively.

Finally, the output vector $\hat{y}_t$ can be obtained as follows:

$$\hat{y}_t = f\left(W_{ym}m_t + b_y\right) \tag{6}$$

where W_{ym} represents the weight matrix, and b_y denotes the bias vector.

2.2.3. Convolutional Neural Network (CNN)

CNN is a prominent subset of DL, extensively utilized in domains including image recognition and natural language processing [38]. By employing trainable filters that traverse input sequences, CNN performs convolution operations to extract spatial features from multidimensional data in Euclidean space [39,40]. When applied to landslide displacement time series, a one-dimensional CNN (1D-CNN) can effectively capture meaningful temporal patterns and features, thereby enhancing the model's generalization performance [18]. The convolution operation is expressed as follows:

$$M_i = f\left(\sum M_{i-1} \cdot W_i + b_i\right) \tag{7}$$

where M_i denotes the input feature map at the ith layer, $f(\cdot)$ represents the activation function, W_i is the convolution kernel weight, and b_i corresponds to the bias term.

2.3. The Proposed Combined Model and Performance Evaluation

2.3.1. Assigning the Cloud Model-Based Combination Weights

The cloud model enables an efficient qualitative-to-quantitative transformation by integrating the expectation *Ex*, entropy *En*, and hyper-entropy *He* [41]. Based on this framework, the cloud model-based combination strategy generally includes four steps and can be shown as follows:

Step 1. Cloud model establishment

Let $X_a = \{x_1, x_2, \cdots, x_N\}$ and $Y = \{y_1, y_2, \cdots, y_N\}$ denote the forecasted and observed displacement sequences. To reduce the dimensionality of the original sequences, both X_a and Y are divided into m sequential segments T_i $(i = 1, 2, \cdots, m)$ of equal length. Each segment is transformed into a normal cloud form using the BCG. Let $V_X \sim (Ex_X,\ En_X,\ He_X)$ and $V_Y \sim (Ex_Y,\ En_Y,\ He_Y)$ denote the cloud models corresponding to segments of X_a and Y over the same period, respectively. The similarity between V_X and V_Y is quantified by the overlapping area S [42], derived from the intersection of expectation curves.

Step 2. Similarity degree computing

The similarity degree $sim(V_X,\ V_Y)$ between two segments can be evaluated as follows [43]:

$$\begin{cases} ol(V_X,\ V_Y) = \frac{2(sup\{C_{1\alpha}\} - inf\{C_{2\alpha}\})}{(sup\{C_{1\alpha}\} - inf\{C_{1\alpha}\}) + (sup\{C_{2\alpha}\} - inf\{C_{2\alpha}\})} \\ sim(V_X,\ V_Y) = \frac{\mu - \alpha}{1 - \alpha} \cdot ol(V_X,\ V_Y) \end{cases} \tag{8}$$

where $ol(V_X,\ V_Y)$ represents the overlap degree. $sup\{C_{i\alpha}\}$ and $inf\{C_{i\alpha}\}$ denote the supremum and infimum of the expectation curve. α corresponds to the cloud model's certainty degree under the "3E" rules, which is determined as 0.0111. μ is the certainty degree of intersection. Let sim_i $(i = 1, 2,\ \cdots, m)$ be the similarity between the T_i, the global similarity between X_a and Y is defined as follows:

$$sim_g(X_a,\ Y) = \sqrt{\frac{1}{m} \cdot \sum_{i=1}^{m} sim_i} \tag{9}$$

Step 3. Combination weight calculating

According to the information fusion similarity, the combination weight for each predictor is given by:

$$\omega_k = \frac{sim_g(X_{ak},\ Y)}{\sum_{k=1}^{M} sim_g(X_{ak},\ Y)},\ (k = 1, 2, \cdots, M) \tag{10}$$

where M is the number of models. ω_k and X_{ak} are the combination weight and forecast result of the kth model, respectively.

Step 4. Individual prediction combining

In this manner, the cloud model-based weighting strategy, which considers the underlying distribution characteristics of the predicted results, is then used to combine individual predictions. The final combined prediction $\hat{y}$ is computed as:

$$\hat{y} = \sum_{k=1}^{M} X_{ak} \cdot \omega_k \tag{11}$$

2.3.2. The Novel Combined Model

The proposed approach is structured in three steps. Figure 1 presents a flowchart that summarizes the proposed combined model.

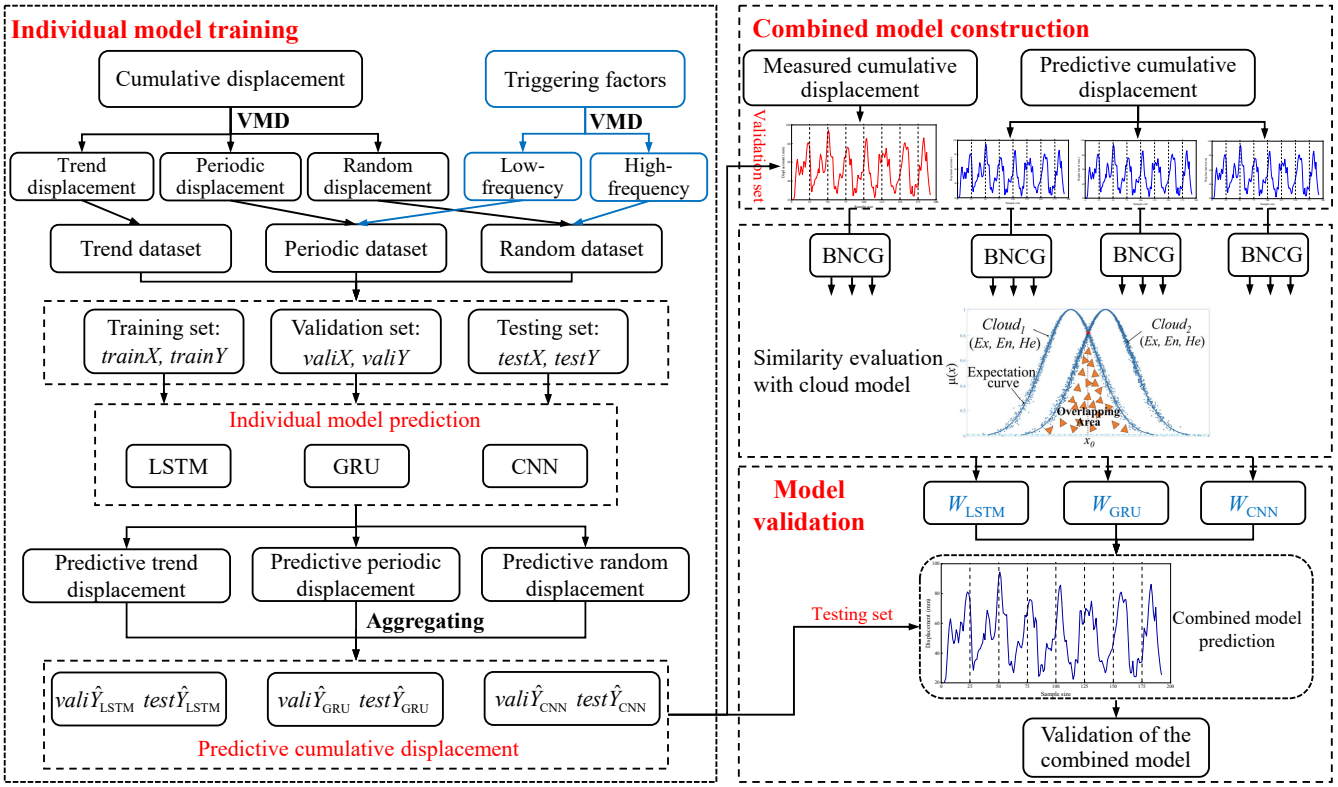


Figure 1. Flowchart of the combined prediction model.

1. The cumulative displacement series is decomposed by VMD into stationary components with unique frequency characteristics, including trend, periodic, and random components. Additionally, the influence factor datasets are decomposed into low- and high-frequency sequences by VMD to construct the initial feature vector for prediction.
2. LSTM, GRU, and CNN are developed as individual forecasting models, and utilized to predict each displacement component separately. The predicted cumulative displacement is subsequently reconstructed by aggregating the predicted values of each component.
3. A cloud model-based combination strategy is employed to dynamically determine the combination weights according to the statistical distribution properties of the forecasted series and to obtain the final displacement.

2.3.3. Triggering Factors of Landslide Displacement

Numerous theoretical studies and analyses indicate that reservoir water level (RWL) fluctuation and seasonal rainfall significantly influence both periodic and random displacement. They can affect the distribution of the hydrodynamic field within the sliding mass and decrease the shear strength [44,45]. Additionally, landslides are time-varying systems that may respond differently to the same external influences at different evolutionary stages [46]. Consequently, RWL, rainfall, and the evolution state are regarded as the primary influence factors:

(1) RWL factors: average elevation of RWL during the current month (R1), RWL variation during the previous 1 month (R2), and the previous 2 months (R3).
(2) Seasonal rainfall: cumulative precipitation of the previous 1 month (P1), and the previous 2 months (P2).
(3) State factor: periodic displacement during the previous 1 month (S1_periodic), 2 months (S2_periodic), and 3 months (S3_periodic), and random displacement during the past 1 month (S1_random), 2 months (S2_random), and 3 months (S3_random).

2.3.4. Model Evaluation Metrics

Four metrics were utilized to assess prediction performance. The corresponding calculation formulas are presented below:

$$1.\text{Root mean square error}: \ RMSE = \sqrt{\sum_{t=1}^{T} (\hat{y}_t - y_t)^2 / T} \tag{12}$$

$$2.\text{Mean absolute error}: \ MAE = \sum_{t=1}^{T} |\hat{y}_t - y_t| / T \tag{13}$$

$$3.\text{Mean absolute percentage error}: \ MAPE = \frac{1}{T} \sum_{t=1}^{T} (|\hat{y}_t - y_t|) / y_t \tag{14}$$

$$4.\text{Relation coefficient}: \ R = \frac{\sum_{t=1}^{T} (y_t - \overline{y})(\hat{y}_t - \hat{y}')}{\sqrt{\sum_{t=1}^{T} (y_t - \overline{y})^2} \sqrt{\sum_{t=1}^{T} (\hat{y}_t - \hat{y}')^2}} \tag{15}$$

where T represents the number of samples. $\hat{y}_t$ refers to the predicted landslide displacement, while y_t corresponds to the actual value. $\hat{y}'$ and $\overline{y}$ denote the mean of predicted and measured values. Notably, superior forecasting accuracy is reflected by lower RMSE, MAE, and MAPE and higher R.

3. Case Study

3.1. Geological Conditions

The Baishuihe landslide is situated on the southern bank of the Yangtze River (Figure 2b). The landslide exhibits a fan-shaped geometry, with its front edge below the 135 m water level, and its back edge situated at approximately 410 m a.s.l (Figure 2a). The geological profile, as depicted in Figure 2c, reveals that the sliding mass primarily consists of Quaternary sediments with a disorganized internal structure. The underlying bedrock is composed predominantly of Jurassic siltstone, quartz sandstone, and arenaceous shale. Geological investigations have identified two potential slip zones within the landslide. The shallow sliding zone, occurring at depths of 12 m to 25 m, is separated from the deeper sliding zone, which lies at the boundary between the underlying carbonaceous mudstone and the basal cataclastic rock.

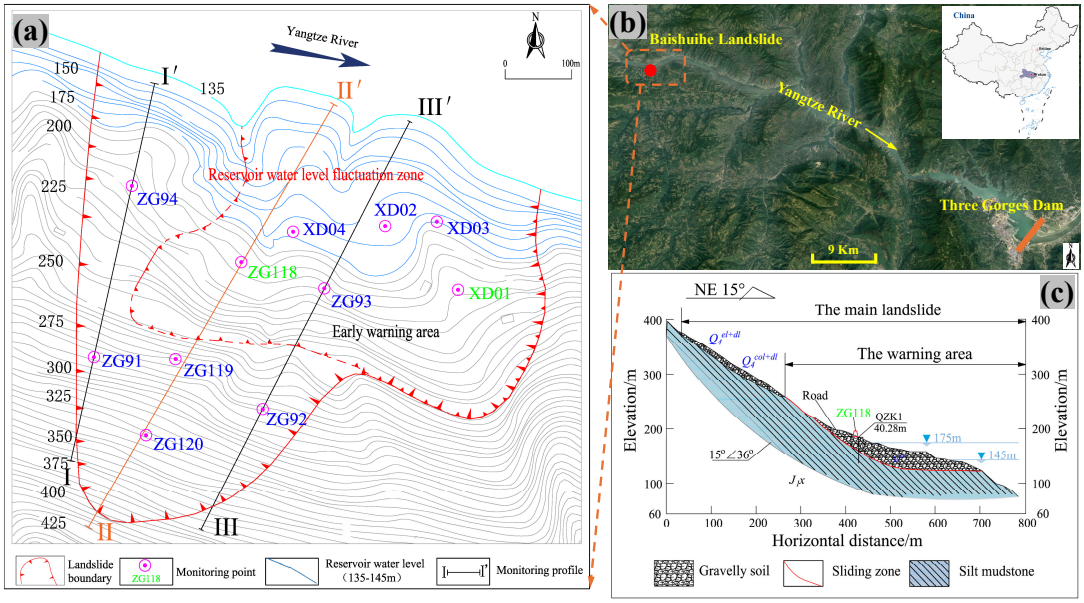


Figure 2. (**a**) Topographic map of the case study landslide. (**b**) Location of the study area. (**c**) Schematic geological cross-section II–II′.

3.2. Landslide Deformation Characteristics Analysis

Site investigations divided the sliding mass into two primary zones: an actively deforming region (early warning area A) and a relatively stable region (area B). As shown in Figure 2a, eleven surface GPS stations were installed across the sliding mass to monitor the displacement monthly (six stations in area A and five stations in area B). The monthly rainfall, RWL, and cumulative displacement at monitoring sites ZG118 and XD01 from 2003 to 2013 are presented in Figure 3. Observations indicate that the landslide remained unstable, undergoing continuous deformation throughout the monitoring period, with total displacements of 2328.9 mm and 3167.0 mm recorded for ZG118 and XD01, respectively. The displacement curves demonstrate a clear step-like pattern, which can be divided into three distinct phases. Specifically, displacement increments corresponding to the hydrological years of 2005, 2006, and 2010–2012 were selected from the three deformation stages for analysis, along with RWL and rainfall data, as illustrated in Figure 4a–c.

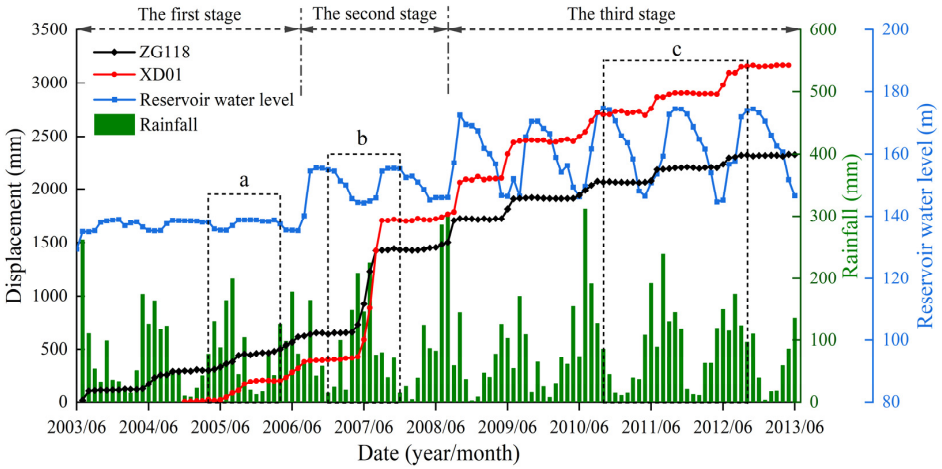


Figure 3. Monthly rainfall, RWL, and displacement at ZG118 and XD01sites. Letters a–c represent the hydrological years of 2005, 2006, and 2010–2012, respectively.

Stage 1: from June 2003 to August 2006. Prior to the initial operation of the TGR, displacement occurred more gradually, exhibiting a strong correlation with seasonal rainfall. The landslide experienced rapid deformation annually, typically from April to September, and remained relatively stable from October to the following April. As shown in Figure 4a, from April 2005 to April 2006, the RWL remained relatively stable, and the deformation increments did not exhibit significant fluctuations in response to RWL changes. However, following peak rainfall in August 2005, the displacement increments at the ZG118 and XD01 sites reached maximum values in September and October, respectively. It indicates that rainfall had a certain impact on deformation with a noticeable lag effect.

Stage 2: from September 2006 to October 2008. During this period, the RWL gradually rose to 156 m and subsequently fluctuated within the interval of 145–156 m. The most significant displacement increase occurred with the initial decline in RWL from 156 to 145 m. As shown in Figure 4b, as the RWL began to significantly decrease in February, no immediate deformation increment was observed. Instead, noticeable displacement occurred starting in April, with a lag period of approximately 1–2 months. When the seasonal rainfall occurred and RWL dropped, deformation increments sharply increased, reaching maximum values of 311.52 mm/month and 538.49 mm/month at ZG118 and XD01, respectively. It indicates that the combined influence of RWL fluctuations and heavy rainfall triggered a sharp deformation increment. As the stress and seepage fields within the sliding mass adjusted to the new reservoir conditions, the deformation rate gradually stabilized, indicating that a new equilibrium state had been reached.

Stage 3: from November 2008 to June 2013. The RWL fluctuated periodically between 145 m and 175 m and the landslide exhibited typical step-like deformation. Figure 4c demon-

strates that, during significant drops in RWL, landslide deformation initially accelerated before gradually stabilizing due to the combined influence of RWL and rainfall.

Overall, the combined effects of RWL decline and rainfall exert an amplifying influence on landslide deformation. The drop in RWL gradually disrupts the stress distribution within the slide mass, diminishing its overall stability. Meanwhile, rainfall rapidly increases the internal water content and pore water pressure, further weakening its shear strength. Thus, the interplay of these two factors, following a lag effect, can trigger large-scale landslide deformation. The interaction mechanism highlights the complexity and multifactorial nature of landslide.

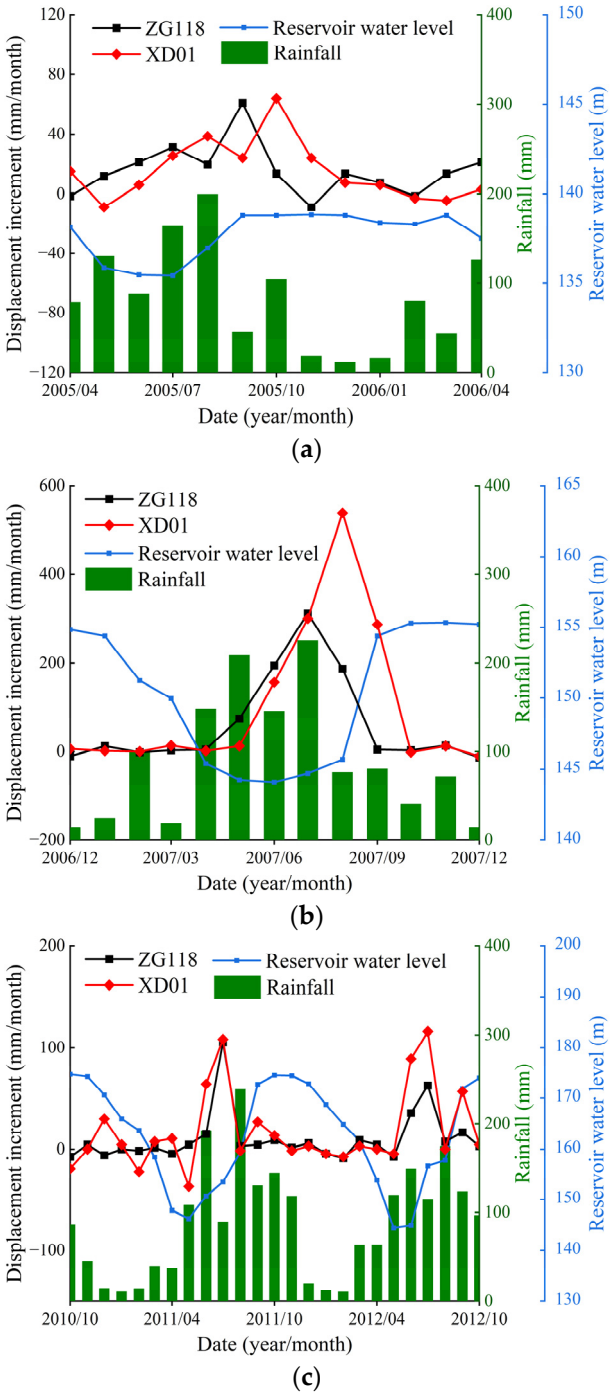


Figure 4. Monthly rainfall, RWL, and displacement increments of the characteristic hydrological years. (**a**) April 2005–April 2006; (**b**) December 2006–December 2007; (**c**) October 2010–October 2012.

4. Results

4.1. Results of Displacement Decomposition

The displacement data from ZG118 and XD01, situated in the early warning area, were adopted for displacement prediction analysis. The dataset collected from June 2003 to December 2011 observed at ZG118 was used to establish and train the models, while data from January 2012 to June 2013 was served for testing. At site XD01, due to the shorter monitoring period, data from December 2004 to December 2011 were employed for training, with data from January 2012 to May 2013 utilized for testing.

The deformation of reservoir landslides arises from the combined influence of geological conditions and periodic hydrodynamic factors. The trend component, characterized by a monotonic curve, primarily reflects the long-term evolution. Periodic displacement, influenced by seasonal rainfall and RWL, exhibits a regular fluctuation pattern. Meanwhile, random displacement is attributed to irregular external influences, including wind loads and seismic activity. According to Equations (1)–(3), the monthly cumulative displacement series was decomposed into K independent modes. Prior to displacement decomposition, the optimal decomposition level (K) was set to 3 to ensure the physical interpretability of each component, and the convergence criterion (ε) was specified as 10^{-7}. Furthermore, the quadratic penalty term (α) and noise tolerance (τ) was determined to be 5.0 and 0.1, respectively, based on a pre-trial analysis of the center frequency iterations. These parameters ensured that the decomposed modes could be reconstructed with minimal noise.

According to the distinct variation characteristics of the decomposed modes, the low-frequency (LF) mode captures the trend evolution, while the intermediate-frequency (IF) mode reflects the periodic fluctuation, and the high-frequency (HF) mode primarily contains random displacement information. Thus, the original displacement series can be decomposed into three independent modes: trend, periodic, and random components. Figure 5 illustrates the decomposition results, with the frequencies of the modes arranged in ascending order. By decomposing the original displacement series, the complexity level of forecasting is significantly reduced, as the data becomes more periodic and regular. The trend displacement shows a consistent upward progression, while periodic displacement shows cyclical fluctuations, and the random displacement fluctuates within a narrow range.

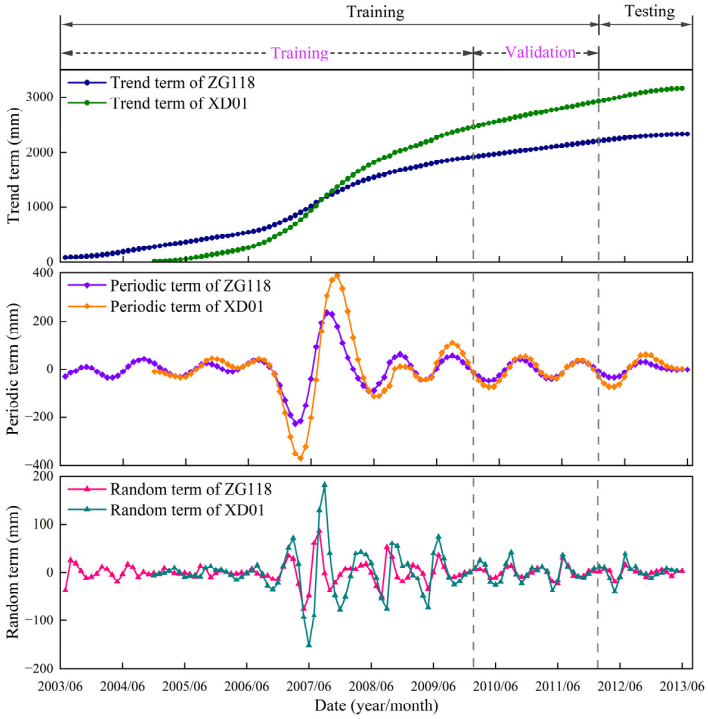


Figure 5. Cumulative displacement decomposition at ZG118 and XD01.

4.2. Results of Trend Displacement Prediction

The evolution state was selected as the primary factor for trend displacement prediction. To achieve this, the trend displacements during the previous month and two months were adopted as input variables, and the current trend displacement served as the output. The one-layer univariate LSTM, GRU, and CNN models were implemented using Keras (https://keras.io/) and Scikit-learn (https://scikit-learn.org/stable/) packages for trend displacement forecasting. Hyperparameters were optimized via grid search (GS) by minimizing RMSE on the validation dataset, resulting in a batch size of 24 and 100 neurons, with other parameters set to default values.

Table 1 summarizes the performance of each model during testing. The predictive trend displacement at ZG118 revealed that the LSTM model provided outstanding performance with the lowest RMSE and MAE of 6.36 mm and 5.95 mm, respectively, whereas the CNN model exhibited the weakest performance, with the highest RMSE and MAE of 15.82 mm and 15.69 mm. The R values for all three models were 0.999. As for the prediction at XD01, the GRU model provided optimal results, with RMSE and MAE of 5.77 mm and 4.56 mm, whereas the CNN model again performed the worst, recording RMSE and MAE of 20.49 mm and 19.56 mm. Regarding R values, CNN and GRU outperformed LSTM, achieving 0.998 compared with 0.997.

Table 1. Performance accuracy of the trend displacement prediction.

Evaluation Indices	ZG118			XD01		
	CNN	**LSTM**	**GRU**	**CNN**	**LSTM**	**GRU**
RMSE/mm	15.82	6.36	9.64	20.49	8.27	5.77
MAE/mm	15.69	5.95	9.25	19.56	6.98	4.56
R	0.999	0.999	0.999	0.998	0.997	0.998

4.3. Results of Periodic and Random Displacement Prediction

4.3.1. Dominant Triggering Variables Selection

The LF components were characterized by obvious periodicity, while the HF components represented random fluctuations in the triggering factor sequences. Therefore, the LF modes of each factor were used as input variables for periodic displacement forecasting, while the HF terms were adopted for random displacement forecasting. An initial database including 16 candidate input variables was then established for model training. The maximum information coefficient (MIC) [47] was utilized to assess the relationships between candidate variables and nonlinear displacements.

A Python-based open-source library minepy 1.2.6 was employed to calculate the MIC values. The analysis results illustrated in Table 2 demonstrate a strong correlation between periodic displacement and the variation in RWL during the past two months (R3), followed by the RWL variation over the past one month (R2). Notably, the MIC of R3 surpassed that of the two rainfall-related factors, suggesting that periodic displacement was predominantly affected by RWL fluctuations over the preceding two months, with rainfall exerting a comparatively smaller influence. Furthermore, the S1_periodic and S2_periodic were identified as the primary state factors, showing the highest correlation with the current periodic displacement. On the other hand, the random displacement component, driven by stochastic factors, demonstrated higher MIC values for the evolutionary state factors compared with those associated with rainfall and RWL, indicating that these state factors significantly influenced the random variation of landslide displacement.

Table 2. The MIC values between influencing factors and periodic versus random displacement.

Triggering Factors	ZG118				XD01			
	Periodic Displacement	MIC	Random Displacement	MIC	Periodic Displacement	MIC	Random Displacement	MIC
Rainfall factors	LF of P1	0.330	HF of P1	0.162	LF of P1	0.200	HF of P1	0.213
	LF of P2	0.179	HF of P2	0.199	LF of P2	0.330	HF of P2	0.219
RWL factors	LF of R1	0.258	HF of R1	0.217	LF of R1	0.317	HF of R1	0.226
	LF of R2	0.467	HF of R2	0.219	LF of R2	0.367	HF of R2	0.262
	LF of R3	0.570	HF of R3	0.193	LF of R3	0.438	HF of R3	0.153
Evolution state factors	S1_periodic	0.613	S1_random	0.201	S1_periodic	0.695	S1_random	0.375
	S2_periodic	0.281	S2_random	0.252	S2_periodic	0.324	S2_random	0.220
	S3_periodic	0.137	S3_random	0.347	S3_periodic	0.184	S3_random	0.471

4.3.2. Predicted Periodic and Random Displacement

Multivariable LSTM, GRU, and CNN models were developed to forecast both periodic and random displacements, and the modeling process can be found in Supplementary Materials. The predictive results of periodic and random displacement at ZG118 and XD01 are presented in Figures 6 and 7. Table 3 summarizes the assessment metrics of each model. Figure 6 illustrates that the predicted periodic displacement generated by LSTM, GRU, and CNN corresponded well with the decomposed values overall at the ZG118 and XD01 sites. Specifically, the predictive periodic displacement at ZG118 revealed that the LSTM model provided outstanding performance, achieving the smallest RMSE and MAE of 5.89 mm and 4.42 mm, whereas the CNN model achieved the weakest performance, with the highest RMSE and MAE of 11.39 mm and 10.75 mm, respectively. As for the prediction at XD01, the LSTM model provided the optimal results, achieving RMSE and MAE of 8.61 mm and 7.03 mm, whereas the CNN model performed worst with RMSE and MAE of 20.58 mm and 16.25 mm, respectively. For random displacement prediction, Figure 7 and Table 3 reveal that the GRU model offered superior performance with the lowest RMSE and MAE of 5.76 mm and 4.70 mm at the ZG118 site, and the CNN model corresponded with the smallest RMSE and the largest R of 11.51 mm and 0.842 at the XD01 site.

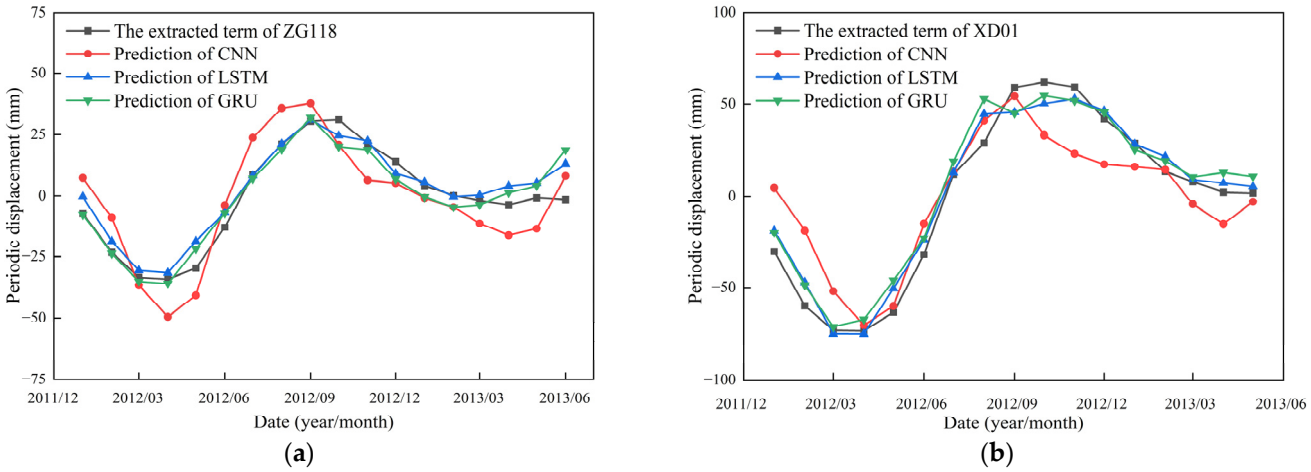


Figure 6. Comparison of measured and predicted periodic displacement during the testing period. (**a**) ZG118; (**b**) XD01.

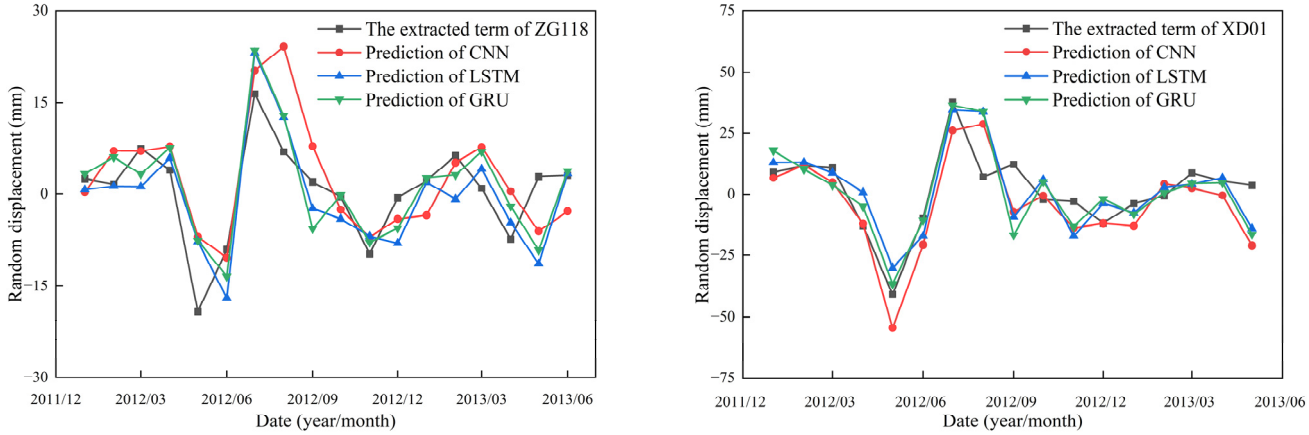


Figure 7. Comparison of measured and predicted random displacement during the testing period. (**a**) ZG118; (**b**) XD01.

Table 3. Prediction performance of individual models for periodic and random displacement.

Monitoring Sites	Individual Models	Periodic Displacement			Random Displacement		
		RMSE/mm	MAE/mm	R	RMSE/mm	MAE/mm	R
ZG118	CNN	11.39	10.75	0.877	6.77	5.37	0.710
	LSTM	5.89	4.42	0.971	6.16	4.89	0.736
	GRU	6.61	4.71	0.942	5.76	4.70	0.759
XD01	CNN	20.58	16.25	0.906	11.51	8.85	0.842
	LSTM	8.61	7.03	0.986	11.55	8.96	0.744
	GRU	10.45	8.91	0.982	12.05	8.57	0.744

4.4. Cumulative Displacement Prediction and Evaluation

By summing the predicted trend, and periodic and random displacements, the cumulative displacement was obtained in accordance with the decomposition–ensemble principle. The forecasting results of cumulative displacement at two sites are shown in Figure 8. A comparison analysis indicated that the prediction of individual models corresponded well to the measured values, and the "step-like" increasing trend in cumulative displacement can be effectively modeled.

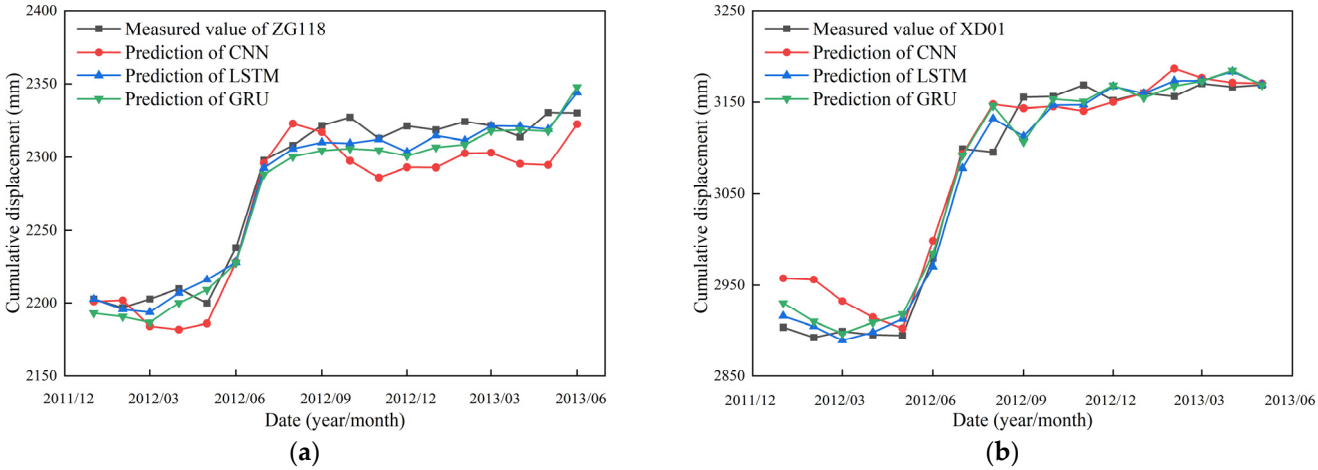


Figure 8. Comparison of the measured and predicted cumulative displacement of individual models. (**a**) ZG118; (**b**) XD01.

Following the framework of the cloud model-based combined prediction model, the validation sequences of the measured and predicted displacements were first-order differential processes and divided into three equal segments in order. Table 4 illustrates the specific digital characteristics of cloud model matching for each segment. These digital features corresponding to each subsequence were then incorporated into the OCEM algorithm to calculate the global similarity between the measured and predicted displacement sequences for individual models. Consequently, the combined model was established and used for cumulative displacement forecasting during the testing period. At the ZG118 station, the global similarities for the CNN, LSTM, and GRU models were determined to be 0.926, 0.903, and 0.909, respectively, with the corresponding combination weights being 0.338, 0.330, and 0.332. At the XD01 site, the global similarities for the CNN, LSTM, and GRU models were 0.927, 0.939, and 0.946, respectively, with the corresponding model combined weights being 0.330, 0.334, and 0.336.

Table 4. Digital characteristics of cloud model matching of each segment.

Sites	Segment	Actual Displacement (*Ex*, *En*, *He*)	Predicted Displacement (*Ex*, *En*, *He*)		
			CNN	LSTM	GRU
ZG118	1	(15.39, 25.44, 1.14)	(13.86, 22.70, 6.29)	(15.16, 20.53, 0.02)	(15.43, 21.68, 1.01)
	2	(2.97, 9.83, 8.28)	(2.12, 12.08, 6.29)	(3.11, 8.19, 5.42)	(3.13, 9.45, 4.65)
	3	(18.54, 26.32, 22.29)	(18.84, 23.33, 14.85)	(17.36, 21.78, 8.51)	(17.38, 18.60, 11.30)
XD01	1	(22.07, 37.12, 7.90)	(24.65, 34.66, 13.48)	(19.31, 35.66, 9.36)	(21.19, 39.12, 10.76)
	2	(11.12, 26.94, 20.07)	(6.77, 23.37, 14.13)	(12.24, 34.89, 4.22)	(9.79, 35.19, 2.43)
	3	(21.88, 42.84, 15.20)	(24.55, 34.30, 16.36)	(23.03, 45.67, 21.20)	(20.98, 42.77, 19.18)

Figure 9 presents a comparison between the observed and combined prediction results at ZG118 and XD01. At both sites, it was observed that the developed combined model provided good performance on tracking and forecasting the increasing evolution of the cumulative displacement overall, with maximum absolute errors below 50.00 mm. Table 5 presents a comparison of the performance metrics between individual models and the combined model. The RMSE, MAPE, and R of the final predictive result at ZG118 were 12.63 mm, 0.46% and 0.987, respectively, while these accuracy indices at XD01 were 20.50 mm, 0.52%, and 0.990. Furthermore, the performance of the combined model at ZG118, which benefited from an extended monitoring period, outperformed that at XD01, which was trained on a more limited sample set.

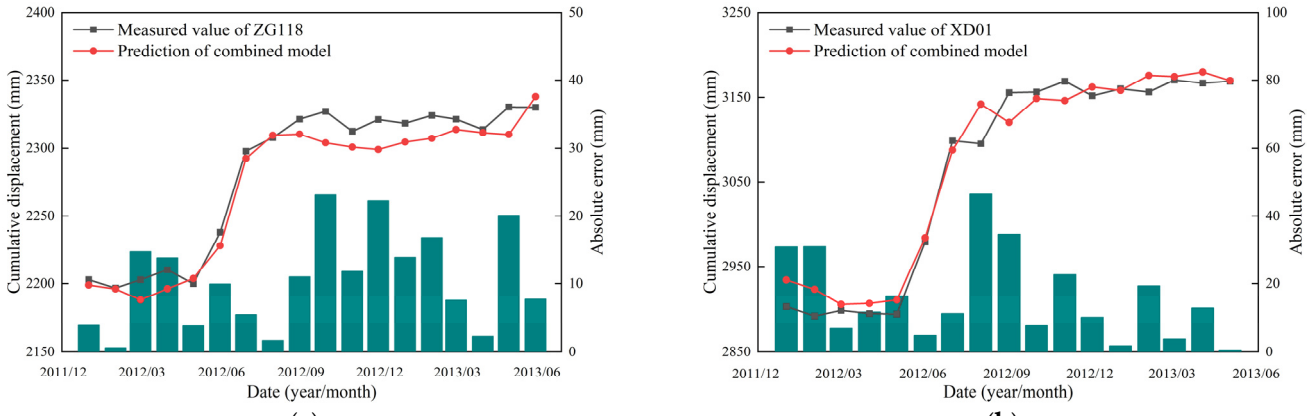


Figure 9. Comparison of the measured and predicted cumulative displacement of combined model. (**a**) ZG118; (**b**) XD01.

Table 5. Prediction performance of cumulative deformation with individual models.

Monitoring Sites	Evaluation Indices	Individual Models			Combined Model
		CNN	LSTM	GRU	
ZG118	RMSE/mm	20.08	10.08	12.86	12.63
	MAPE/%	0.75	0.35	0.52	0.46
	R	0.968	0.985	0.983	0.987
XD01	RMSE/mm	28.47	18.48	21.51	20.50
	MAPE/%	0.69	0.48	0.52	0.52
	R	0.983	0.988	0.985	0.990

5. Discussion

5.1. Combined Model Improves Prediction Accuracy

Previous research has shown that no single model can accurately predict all displacement components, as each model excels in specific aspects. For instance, the LSTM model demonstrated superior predictive performance for periodic components at the ZG118 and XD01 monitoring stations, while the GRU and CNN models were better suited for forecasting random displacement. In terms of cumulative displacement prediction, all three models performed well across different phases, including the early warning period (i.e., the stepwise rapid deformation stage) and more stable periods. This suggests that the three models are reliable and should be prioritized for displacement forecasting in reservoir landslides. Additionally, several predictive models have been proposed for the ZG118 and XD01 sites in previous studies, and the forecasting results of the combined model were compared with those of advanced approaches, including PSO-GSA-SVR [48], VMD-GWO-MIC-SVR [49], and VMD-Stacked LSTM-TAR [50]. For cumulative displacement at the ZG118 site, with the same training samples, the RMSE values for PSO-GSA-SVR, VMD-GWO-MIC-SVR, and VMD-Stacked LSTM-TAR were 11.09 mm, 17.02 mm, and 16.80 mm, respectively, thereby validating that the combined model achieves competitive predictive performance.

To maintain the accuracy of model predictions and the reliability of early warning systems, it is essential to continuously update models with the latest data and extract new information. Although these models generally perform well, sudden variations in influencing factors, such as rainfall intensity and RWL, can increase prediction errors at specific points. Improving accuracy requires integrating recent monitoring data while gradually phasing out outdated information. This approach enhances precision in identifying causal relationships, ultimately improving the reliability of early warning systems.

5.2. Reservoir Operation Impacts Landslide Displacement

The stepwise deformation behavior of landslides is mainly driven by the interplay of external periodic forces, including RWL fluctuations and rainfall. However, the landslide's response to these factors varies noticeably across different stages of deformation evolution. Specifically, the landslide deformation exhibits two distinct phases within a hydrological year: a stable creep stage and an accelerating deformation stage. This observation underscores the need for a thorough analysis of the mechanisms governing each evolutionary stage. By applying the VMD method to the cumulative displacement and potential impact factor sequences, the periodic fluctuations and frequency characteristics of both deformation and influencing factors are extracted. On this basis, initial related factors are selected with the objective of identifying the relationship between RWL, rainfall-related factors, and the decomposed periodic displacement using the MIC algorithm. The results of both qualitative analysis and correlation studies suggest that rainfall serves as the primary driving factor for the landslide, whereas RWL acts as the main contributing factor. Furthermore, the periodic deformation displays a stronger correlation with RWL fluctuations occurring in the preceding one or two months, particularly during periods of RWL decline. Given the strong correlation between RWL fluctuations and periodic landslide displacement, from a reservoir management perspective, gradual adjustments of RWL at a relatively

slow rate are recommended. Such adjustments help stabilize slopes by preventing rapid changes in pore pressure and reducing the hydrodynamic forces exerted on the sliding mass. Additionally, scheduling reservoir drawdowns during periods of anticipated heavy rainfall could mitigate the combined destabilizing effects of high RWL and precipitation.

5.3. Limitations and Future Directions

This study proposes a cloud model-based combined strategy to enhance prediction accuracy and robustness. Despite promising results, several limitations remain that future research should address. A primary limitation is the reliance on a limited dataset, which may impact the model's generalizability to other landslide-prone regions with diverse geological conditions. Additionally, the VMD-based decomposition process requires careful parameter selection, potentially affecting consistency across datasets. The accuracy of the combined result is also influenced by the effectiveness of individual methods, with occasional errors from poorly suited predictors possibly affecting the overall model's effectiveness. Future research could explore hybrid VMD techniques, such as combining VMD with other decomposition methods to improve mode separation accuracy. Additionally, evaluating and filtering out low-performing predictors in advance could enhance the combined model's reliability. Incorporating advanced deep learning architectures, like transformer models, may further improve forecasting by capturing complex temporal dependencies. Finally, testing this approach on landslide datasets from varied geological regions would help validate its generalizability.

6. Conclusions

Forecasting landslide displacement triggered by periodic hydrodynamic factors is essential for maintaining the safe operation of hydropower stations in the TGR area. Considering the inherent dynamic characteristics of a reservoir landslide displacement sequence, this research proposes a hybrid framework for displacement forecasting based on VMD, three DL algorithms, and a cloud model-based combined module to enhance the predictive capability. Using the monitored dataset collected from the Baishuihe landslide, the developed combined model performed well in displacement forecasting by considering the effects of rainfall and RWL. The main results are outlined as follows:

(1) Qualitative and quantitative analyses of displacement evolution and external influence factors reveal that the step-like deformation characteristics are primarily induced by seasonal rainfall and periodic RWL scheduling. The model leverages the VMD technique to effectively extract deformation components corresponding to various frequency characteristics and achieve clearer physical meaning, demonstrating a superior ability to maintain mode separation without mode mixing and better adaptability to non-stationary data. Additionally, the MIC method was successfully used to identify the relevant causal factors for model establishment, further enhancing its physical interpretability.

(2) The prediction results demonstrate that the established multifactor CNN, LSTM, and GRU models effectively model the step-like increasing trend in cumulative displacement. On this basis, the cloud-model based combination strategy integrates the advantages of individual models, further improving forecasting accuracy.

(3) The proposed combined model is applied to forecast displacement series at the ZG118 and XD01 sites. Results demonstrate robust forecasting performance, with RMSE, MAPE, and R values of 12.63 mm, 0.46%, and 0.987 at ZG118, and 20.50 mm, 0.52%, and 0.990 at XD01, respectively. Overall, this combined modeling approach achieves accurate and reliable predictions for step-like reservoir landslides, showing potential for broader application in predicting landslide displacement within the TGR area and other landslide-prone regions.

Supplementary Materials: The following supporting information can be downloaded at: https://www.mdpi.com/article/10.3390/w16233503/s1. Table S1: Optimal parameters of LSTM, GRU and CNN prediction models.

Author Contributions: Conceptualization, Y.G.; methodology, M.S.; software, M.S. and K.H.; validation, L.Y.; writing—original draft preparation, M.S.; writing—review and editing, Y.G.; visualization, L.Y.; supervision, Y.G. All authors have read and agreed to the published version of the manuscript.

Funding: This research was funded by the Natural Science Foundation of Zhejiang province, China (Grant No. LY23E090001).

Data Availability Statement: The data that support the findings of this study are available on request from the corresponding author upon reasonable request.

Conflicts of Interest: Mengcheng Sun and Ke Huang were employed by Powerchina Huadong Engineering Corporation Limited. The remaining authors declare that the research was conducted in the absence of any commercial or financial relationships that could be construed as a potential conflict of interest.

References

1. Pecoraro, G.; Calvello, M.; Piciullo, L. Monitoring strategies for local landslide early warning systems. *Landslides* **2019**, *16*, 213–231. [CrossRef]
2. Gómez, D.; García, E.F.; Aristizábal, E. Spatial and temporal landslide distributions using global and open landslide databases. *Nat. Hazards* **2023**, *117*, 25–55. [CrossRef]
3. Gupta, K.; Satyam, N. Integrating real-time sensor data for improved hydrogeotechnical modelling in landslide early warning in Western Himalaya. *Eng. Geol.* **2024**, *338*, 107630. [CrossRef]
4. Jia, W.; Wen, T.; Li, D.; Guo, W.; Quan, Z.; Wang, Y.; Huang, D.; Hu, M. Landslide displacement prediction of Shuping landslide combining PSO and LSSVM model. *Water* **2023**, *15*, 612. [CrossRef]
5. Valletta, A.; Carri, A.; Segalini, A. Alert threshold assessment based on equivalent displacements for the identification of potentially critical landslide events. *Nat. Hazards* **2023**, *115*, 1549–1570. [CrossRef]
6. Wei, X.; Zhang, L.; Gardoni, P.; Chen, Y.; Tan, L.; Liu, D.; Du, C.; Li, H. Comparison of hybrid data-driven and physical models for landslide susceptibility mapping at regional scales. *Acta Geotech.* **2023**, *18*, 4453–4476. [CrossRef]
7. Hu, S.; Qiu, H.; Wang, N.; Wang, X.; Ma, S.; Yang, D.; Wei, N.; Liu, Z.; Shen, Y.; Cao, M. Movement process, geomorphological changes, and influencing factors of a reactivated loess landslide on the right bank of the middle of the Yellow River, China. *Landslides* **2022**, *19*, 1265–1295. [CrossRef]
8. Wang, Y.; Tang, H.; Huang, J.; Wen, T.; Ma, J.; Zhang, J. A comparative study of different machine learning methods for reservoir landslide displacement prediction. *Eng. Geol.* **2022**, *298*, 106544. [CrossRef]
9. Zhang, L.; Chen, X.; Zhang, Y.; Wu, F.; Chen, F.; Wang, W.; Guo, F. Application of GWO-ELM model to prediction of Caojiatuo landslide displacement in the Three Gorge Reservoir Area. *Water* **2020**, *12*, 1860. [CrossRef]
10. Li, P.; Zha, Y.; Shi, L.; Tso, C.-H.M.; Zhang, Y.; Zeng, W. Comparison of the use of a physical-based model with data assimilation and machine learning methods for simulating soil water dynamics. *J. Hydrol.* **2020**, *584*, 124692. [CrossRef]
11. Guo, Z.; Chen, L.; Gui, L.; Du, J.; Yin, K.; Do, H.M. Landslide displacement prediction based on variational mode decomposition and WA-GWO-BP model. *Landslides* **2020**, *17*, 567–583. [CrossRef]
12. Ge, Q.; Wang, J.; Liu, C.; Wang, X.; Deng, Y.; Li, J. Integrating feature selection with machine learning for accurate reservoir landslide displacement prediction. *Water* **2024**, *16*, 2152. [CrossRef]
13. Zhang, J.; Tang, H.; Tannant, D.D.; Lin, C.; Xia, D.; Liu, X.; Zhang, Y.; Ma, J. Combined forecasting model with CEEMD-LCSS reconstruction and the ABC-SVR method for landslide displacement prediction. *J. Clean. Prod.* **2021**, *293*, 126205. [CrossRef]
14. Zhang, W.; Wu, C.; Tang, L.; Gu, X.; Wang, L. Efficient time-variant reliability analysis of Bazimen landslide in the Three Gorges Reservoir Area using XGBoost and LightGBM algorithms. *Gondwana Res.* **2023**, *123*, 41–53. [CrossRef]
15. Du, H.; Song, D.; Chen, Z.; Shu, H.; Guo, Z. Prediction model oriented for landslide displacement with step-like curve by applying ensemble empirical mode decomposition and the PSO-ELM method. *J. Clean. Prod.* **2020**, *270*, 122248. [CrossRef]
16. Meng, Y.; Qin, Y.; Cai, Z.; Tian, B.; Yuan, C.; Zhang, X.; Zuo, Q. Dynamic forecast model for landslide displacement with step-like deformation by applying GRU with EMD and error correction. *Bull. Eng. Geol. Environ.* **2023**, *82*, 211. [CrossRef]
17. Yang, B.; Yin, K.; Lacasse, S.; Liu, Z. Time series analysis and long short-term memory neural network to predict landslide displacement. *Landslides* **2019**, *16*, 677–694. [CrossRef]
18. Nava, L.; Carraro, E.; Reyes-Carmona, C.; Puliero, S.; Bhuyan, K.; Rosi, A.; Monserrat, O.; Floris, M.; Meena, S.R.; Galve, J.P. Landslide displacement forecasting using deep learning and monitoring data across selected sites. *Landslides* **2023**, *20*, 2111–2129. [CrossRef]
19. Sekhar, C.; Dahiya, R. Robust framework based on hybrid deep learning approach for short term load forecasting of building electricity demand. *Energy* **2023**, *268*, 126660. [CrossRef]

20. Meng, S.; Shi, Z.; Li, G.; Peng, M.; Liu, L.; Zheng, H.; Zhou, C. A novel deep learning framework for landslide susceptibility assessment using improved deep belief networks with the intelligent optimization algorithm. *Comput. Geotech.* **2024**, *167*, 106106. [CrossRef]
21. Latif, S.D.; Ahmed, A.N. Streamflow prediction utilizing deep learning and machine learning algorithms for sustainable water supply management. *Water Resour. Manage.* **2023**, *37*, 3227–3241. [CrossRef]
22. Song, K.; Yang, H.; Liang, D.; Chen, L.; Jaboyedoff, M. Step-like displacement prediction and failure mechanism analysis of slow-moving reservoir landslide. *J. Hydrol.* **2024**, *628*, 130588. [CrossRef]
23. Barjasteh, A.; Ghafouri, S.H.; Hashemi, M. A hybrid model based on discrete wavelet transform (DWT) and bidirectional recurrent neural networks for wind speed prediction. *Eng. Appl. Artif. Intell.* **2024**, *127*, 107340. [CrossRef]
24. Wei, H.; Wang, Y.; Liu, J.; Cao, Y. Monthly runoff prediction by combined models based on secondary decomposition at the Wulong Hydrological Station in the Yangtze River Basin. *Water* **2023**, *15*, 3717. [CrossRef]
25. Li, X.; Guo, M.; Zhang, R.; Chen, G. A data-driven prediction model for maximum pitting corrosion depth of subsea oil pipelines using SSA-LSTM approach. *Ocean Eng.* **2022**, *261*, 112062. [CrossRef]
26. Xu, S.; Niu, R. Displacement prediction of Baijiabao landslide based on empirical mode decomposition and long short-term memory neural network in Three Gorges area, China. *Comput. Geosci.* **2018**, *111*, 87–96. [CrossRef]
27. Guo, Y.; Xu, Y.-P.; Xie, J.; Chen, H.; Si, Y.; Liu, J. A weights combined model for middle and long-term streamflow forecasts and its value to hydropower maximization. *J. Hydrol.* **2021**, *602*, 126794. [CrossRef]
28. Shang, Z.; Chen, Y.; Chen, Y.; Guo, Z.; Yang, Y. Decomposition-based wind speed forecasting model using causal convolutional network and attention mechanism. *Expert Syst. Appl.* **2023**, *223*, 119878. [CrossRef]
29. Meng, E.; Huang, S.; Huang, Q.; Fang, W.; Wang, H.; Leng, G.; Wang, L.; Liang, H. A hybrid VMD-SVM model for practical streamflow prediction using an innovative input selection framework. *Water Resour. Manag.* **2021**, *35*, 1321–1337. [CrossRef]
30. Wen, C.; Tian, H.; Zeng, X.; Xia, X.; Hu, X.; Pang, B. Landslide Deformation Analysis and Prediction with a VMD-SA-LSTM Combined Model. *Water* **2024**, *16*, 2945. [CrossRef]
31. Liu, Z.; Jiang, P.; Zhang, L.; Niu, X. A combined forecasting model for time series: Application to short-term wind speed forecasting. *Appl. Energy* **2020**, *259*, 114137. [CrossRef]
32. Duan, J.; Wang, P.; Ma, W.; Fang, S.; Hou, Z. A novel hybrid model based on nonlinear weighted combination for short-term wind power forecasting. *Int. J. Electr. Power Energy Syst.* **2022**, *134*, 107452. [CrossRef]
33. Wang, X.; Hyndman, R.J.; Li, F.; Kang, Y. Forecast combinations: An over 50-year review. *Int. J. Forecast.* **2023**, *39*, 1518–1547. [CrossRef]
34. Li, Y.; Sun, Y.; Wang, Q.; Sun, K.; Li, K.-J.; Zhang, Y. Probabilistic harmonic forecasting of the distribution system considering time-varying uncertainties of the distributed energy resources and electrical loads. *Appl. Energy* **2023**, *329*, 120298. [CrossRef]
35. Dragomiretskiy, K.; Zosso, D. Variational mode decomposition. *IEEE Trans. Signal Process.* **2013**, *62*, 531–544. [CrossRef]
36. Hochreiter, S.; Schmidhuber, J. Long Short-Term Memory. *Neural Comput.* **1997**, *9*, 1735–1780. [CrossRef]
37. Chung, J.; Gulcehre, C.; Cho, K.; Bengio, Y. Empirical evaluation of gated recurrent neural networks on sequence modeling. *arXiv* **2014**, arXiv:1412.3555.
38. Gu, J.; Wang, Z.; Kuen, J.; Ma, L.; Shahroudy, A.; Shuai, B.; Liu, T.; Wang, X.; Wang, G.; Cai, J. Recent advances in convolutional neural networks. *Pattern Recognit.* **2018**, *77*, 354–377. [CrossRef]
39. Khan, A.; Sohail, A.; Zahoora, U.; Qureshi, A.S. A survey of the recent architectures of deep convolutional neural networks. *Artif. Intell. Rev.* **2020**, *53*, 5455–5516. [CrossRef]
40. Li, Z.; Liu, F.; Yang, W.; Peng, S.; Zhou, J. A survey of convolutional neural networks: Analysis, applications, and prospects. *IEEE Trans. Neural Netw. Learn. Syst.* **2021**, *33*, 6999–7019. [CrossRef]
41. Guo, Y.; Xu, Y.P.; Yu, X.; Liu, L.; Gu, H. AI-based ensemble flood forecasts and its implementation in multi-objective robust optimization operation for reservoir flood control. *Water Resour. Res.* **2024**, *60*, e2023WR035693. [CrossRef]
42. Yan, G.; Jia, S.; Ding, J.; Xu, X.; Pang, Y. A time series forecasting based on cloud model similarity measurement. *Soft Comput.* **2019**, *23*, 5443–5454. [CrossRef]
43. Sun, N.; Chen, Z.; Niu, Y.; Yan, G. Similarity measurement between cloud models based on overlap degree. *J. Comput. Appl.* **2015**, *35*, 1955.
44. Du, J.; Yin, K.; Lacasse, S. Displacement prediction in colluvial landslides, three Gorges reservoir, China. *Landslides* **2013**, *10*, 203–218. [CrossRef]
45. Miao, F.; Wu, Y.; Xie, Y.; Li, Y. Prediction of landslide displacement with step-like behavior based on multialgorithm optimization and a support vector regression model. *Landslides* **2018**, *15*, 475–488. [CrossRef]
46. Liu, Y.; Xu, C.; Huang, B.; Ren, X.; Liu, C.; Hu, B.; Chen, Z. Landslide displacement prediction based on multi-source data fusion and sensitivity states. *Eng. Geol.* **2020**, *271*, 105608. [CrossRef]
47. Reshef, D.N.; Reshef, Y.A.; Finucane, H.K.; Grossman, S.R.; McVean, G.; Turnbaugh, P.J.; Lander, E.S.; Mitzenmacher, M.; Sabeti, P.C. Detecting novel associations in large data sets. *Science* **2011**, *334*, 1518–1524. [CrossRef]
48. Xiang, X.; Xiao, J.; Wen, H.; Li, Z.; Huang, J. Prediction of landslide step-like displacement using factor preprocessing-based hybrid optimized SVR model in the Three Gorges Reservoir, China. *Gondwana Res.* **2024**, *126*, 289–304. [CrossRef]

49. Li, L.; Wu, Y.; Miao, F.; Liao, K.; Zhang, L. Displacement prediction of landslides based on variational mode decomposition and GWO-MIC-SVR model. *Chin. J. Rock. Mech. Eng.* **2018**, *37*, 1395–1406.
50. Gao, Y.; Chen, X.; Tu, R.; Chen, G.; Luo, T.; Xue, D. Prediction of landslide displacement based on the combined VMD-stacked LSTM-TAR model. *Remote Sens.* **2022**, *14*, 1164. [CrossRef]

Disclaimer/Publisher's Note: The statements, opinions and data contained in all publications are solely those of the individual author(s) and contributor(s) and not of MDPI and/or the editor(s). MDPI and/or the editor(s) disclaim responsibility for any injury to people or property resulting from any ideas, methods, instructions or products referred to in the content.